



# Self doping promoted photocatalytic removal of NO under visible light with Bi<sub>2</sub>MoO<sub>6</sub>: Indispensable role of superoxide ions



Xing Ding<sup>a,b</sup>, Wingkei Ho<sup>a,\*</sup>, Jian Shang<sup>c</sup>, Lizhi Zhang<sup>c</sup>

<sup>a</sup> Department of Science & Environmental Studies and Center for Education in Environmental Sustainability, The Hong Kong Institute of Education, Hong Kong, PR China

<sup>b</sup> College of Science, Huazhong Agricultural University, Wuhan 430070, PR China

<sup>c</sup> Key Laboratory of Pesticide & Chemical Biology of Ministry of Education, Institute of Environmental Chemistry, College of Chemistry, Central China Normal University, Wuhan 430079, PR China

## ARTICLE INFO

### Article history:

Received 27 July 2015

Received in revised form

18 September 2015

Accepted 21 September 2015

Available online 26 September 2015

### Keywords:

Photocatalytic

Self doping

Bi<sub>2</sub>MoO<sub>6</sub>

Visible light

NO

## ABSTRACT

In this study, we demonstrated that the reactive species generation of Bi<sub>2</sub>MoO<sub>6</sub> under visible light can be regulated by Bi self-doping via a simple soft-chemical method. Density functional theory calculations and systematical characterization results revealed that Bi self-doping could not only promote the separation and transfer of photogenerated electron-hole pairs of Bi<sub>2</sub>MoO<sub>6</sub> but also alter the position of valence and conduction band without changing its preferential crystal orientations, morphology, visible light absorption as well as band gap energy. The photocatalytic removal of NO and products determination revealed that the enhanced generation of superoxide could improve the oxidation of NO to NO<sub>2</sub> while •OH and photogenerated holes mainly contributed to the further oxidation of NO<sub>2</sub> to NO<sub>3</sub><sup>−</sup>. Photostability and NO absorption tests demonstrated that NO<sub>3</sub><sup>−</sup> on the surface of catalysts occupied the NO absorption sites and caused the deactivation of catalysts. This study provides new insight into the different effects of photogenerated reactive species on NO removal and sheds light on the design of highly efficient visible light-driven photocatalysts for NO removal.

© 2015 Elsevier B.V. All rights reserved.

## 1. Introduction

Nitric oxide (NO), mainly produced from internal combustion engines and furnaces, has raised many concerns recently because of its alarming releasing rate in urban environments [1,2]. It has been found to be one of the most common gaseous pollutants in the indoor environment and a major contributor for atmospheric environmental problems such as haze, photochemical smog, acid rain, and so on [3,4]. It was also considered to be a significant risk factor for a number of health conditions, including respiratory infections, heart disease, COPD, stroke, and lung cancer, which seriously threatened the survival of human beings [5–9]. Numerous technologies have been explored for NO purification including wet scrubbing, biofiltration, selective catalytic reduction, photocatalysis, and so on [10–12]. Among them, semiconductor photocatalysis has sparked worldwide interest because of its facility, high efficiency, as well as its potential applications in both aquatic and atmospheric purification [9].

Two common pathways have been proposed during the NO photocatalytic removal process, including photo-selective catalytic reduction (photo-SCR) of NO to N<sub>2</sub> and the oxidation of NO to NO<sub>3</sub><sup>−</sup> with NO<sub>2</sub> as an intermediate. Generally, it is hard to realize NO photoreduction economically at normal temperatures and pressures because of the high activation energy of NO decomposition (Eq. (1),  $E_a = 364 \text{ kJ mol}^{-1}$ ). For instance, Wu and van de Krol found that the NO photoreduction efficiency could only be enhanced from 1% to 4.5% over nanostructured TiO<sub>2</sub> under UV light irradiation through the doping of Fe<sup>3+</sup> in TiO<sub>2</sub> to stabilize the oxygen vacancies [13]. In addition, hydrocarbons or NH<sub>3</sub> was often applied as the reducing agent and added to enhance the NO reduction efficiency. However, some poisonous gas like HCN, HCHO or N<sub>2</sub>O might appear as intermediate by-products and cause secondary emission [14–16]. Besides photo-SCR, NO photocatalytic oxidation is mainly reported to be the major process in NO photocatalytic removal, in which NO was directly oxidized into NO<sub>3</sub><sup>−</sup> by some oxidative species generated under the excitation of solar light such as photogenerated holes, •OH and •O<sub>2</sub><sup>−</sup> radicals (Eqs. (2)–(7)) [2,17–21]. For example, Li et al. found that direct hole transfers and •O<sub>2</sub><sup>−</sup> radical oxidation reaction mainly governed the photocatalytic oxidation of NO over three-dimensional hierarchical bismuth tungstate [4]. Furthermore, •O<sub>2</sub><sup>−</sup>

\* Corresponding author. Fax: +86 852 2948 8255.  
E-mail address: [keithho@ied.edu.hk](mailto:keithho@ied.edu.hk) (W. Ho).

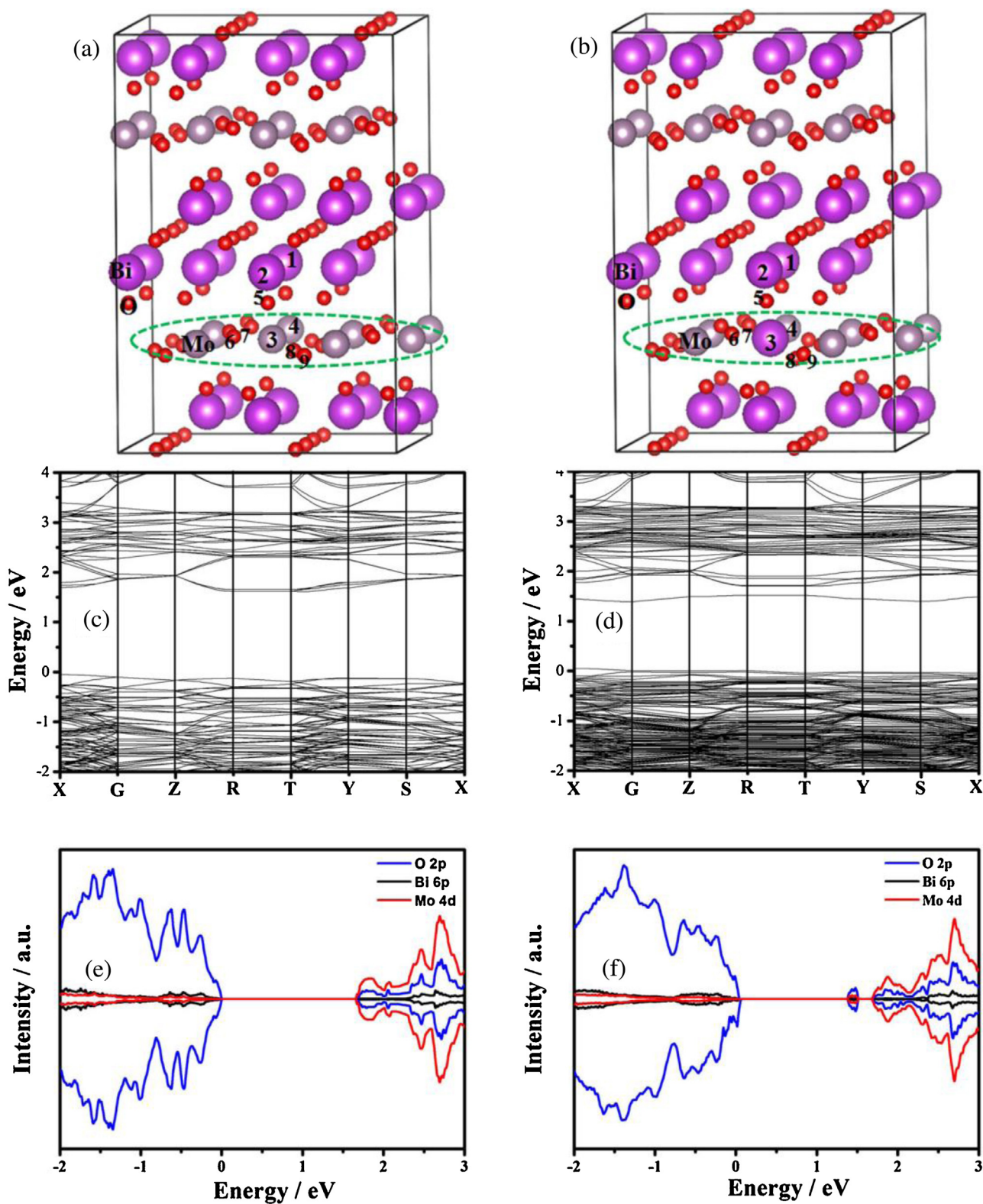
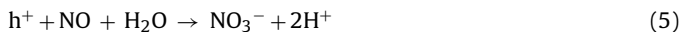


**Fig. 1.** Crystal structures of the pristine (a) and self-doped (b) Bi<sub>2</sub>MoO<sub>6</sub>; calculated band structures of the pristine (c) and self-doped (d) Bi<sub>2</sub>MoO<sub>6</sub>; and total density of states (DOS) of the pristine (e) and self-doped (f) Bi<sub>2</sub>MoO<sub>6</sub>.

was demonstrated to be as the major main reactive radical while •OH plays a minor function in photocatalytic oxidation of NO over an immobilized polymeric g-C<sub>3</sub>N<sub>4</sub> on Al<sub>2</sub>O<sub>3</sub> ceramic foam under visible light illumination [19]. However, it is still unclear how these oxidative species collaborate with each other and thus influence the

photocatalytic removal efficiency of NO, because the types and the amounts of these active species are not easily modulated during the photocatalysis.





Currently, self-doping has increasingly captured people's attention for it could tune the electronic structures and extend the photo response range, thereby enhancing the photocatalytic activity of semiconductors without introducing foreign elements [22–26]. It was successfully utilized in  $\text{TiO}_2$ ,  $\text{C}_3\text{N}_4$ ,  $\text{BiOI}$  modification and enhanced their photocatalytic activity observably under visible light irradiation by altering their electronic structures [27–29]. In our previous study, we investigated photocatalytic degradation of PCP over Bi self-doped  $\text{Bi}_2\text{WO}_6$  under visible light irradiation and found that self-doping can greatly enhance the generation of  $\cdot\text{O}_2^-$  without alter the formation of  $\cdot\text{OH}$ , which realized the deep mineralization of PCP by modulating the generation of reductive and oxidative species. These research works indicated that self-doping technique might be an efficient method to modulate the active species formation on photocatalysts.  $\text{Bi}_2\text{MoO}_6$ , with a unique layered Aurivillius structure like  $\text{Bi}_2\text{WO}_6$  but possessing superior photocatalytic activity in visible light, is a promising photocatalysts because of its intrinsic chemical inertness, nontoxicity as well as its superior spectral properties [30]. Moreover, it was found to possess an active and selective application in heterogeneous catalysis

and superior performance in water splitting and photodegradation of numerous hardly biodegradable organic pollutants [31,32]. All these superior characteristics indicate  $\text{Bi}_2\text{MoO}_6$  is an excellent candidate for investigating the mechanism of various reactive species on NO removal.

In this study, we developed a simple soft-chemical method to realize Bi self-doping of  $\text{Bi}_2\text{MoO}_6$ . Density functional theory (DFT) calculations and systematical characterizations were employed to investigate the influence of Bi self doping on the electronic band structures, optical properties, the separation and transfer of photo-generated electron–hole pairs of  $\text{Bi}_2\text{MoO}_6$ , as well as the reactive species generation during photocatalysis. Photocatalytic removal of NO under visible light was utilized to evaluate the photocatalytic activity of as-prepared  $\text{Bi}_2\text{MoO}_6$  samples. Active species trapping experiments were carried out to compare and investigate the contributions of different reactive species during NO removal over  $\text{Bi}_2\text{MoO}_6$  after Bi self-doping. Determination of  $\text{NO}_2$  and  $\text{NO}_3^-$  was employed to check the specific functions of the reactive species during the photocatalytic treatment of NO. Photochemical stability and NO absorption tests were carried out to find out the deactivation cause and the effective regeneration method of self-doped  $\text{Bi}_2\text{MoO}_6$ .

## 2. Experimental

### 2.1. Sample preparation

All reagents used in this work were of analytical grade and used without further purification. In a typical synthesis,  $\text{Bi}(\text{NO}_3)_3 \times 5\text{H}_2\text{O}$

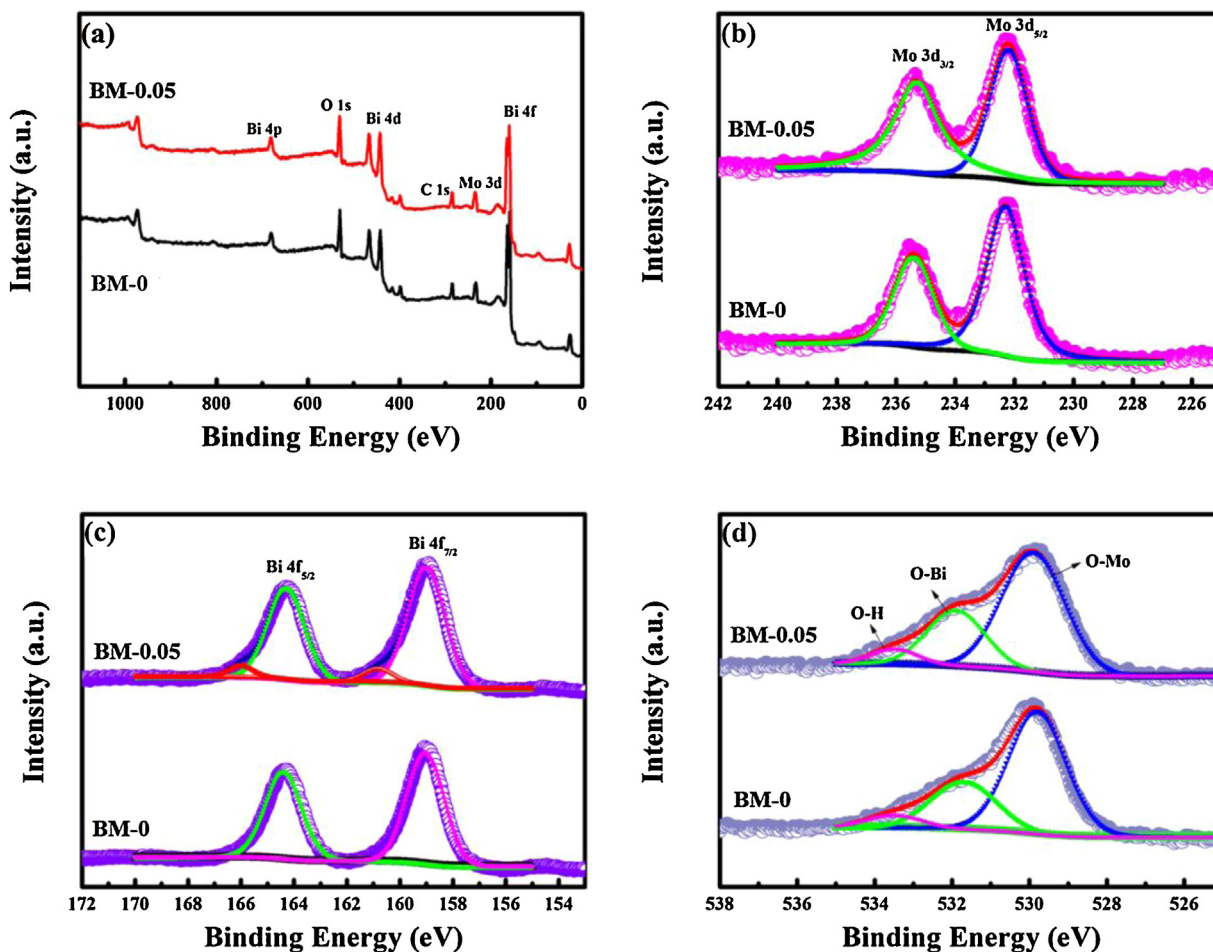
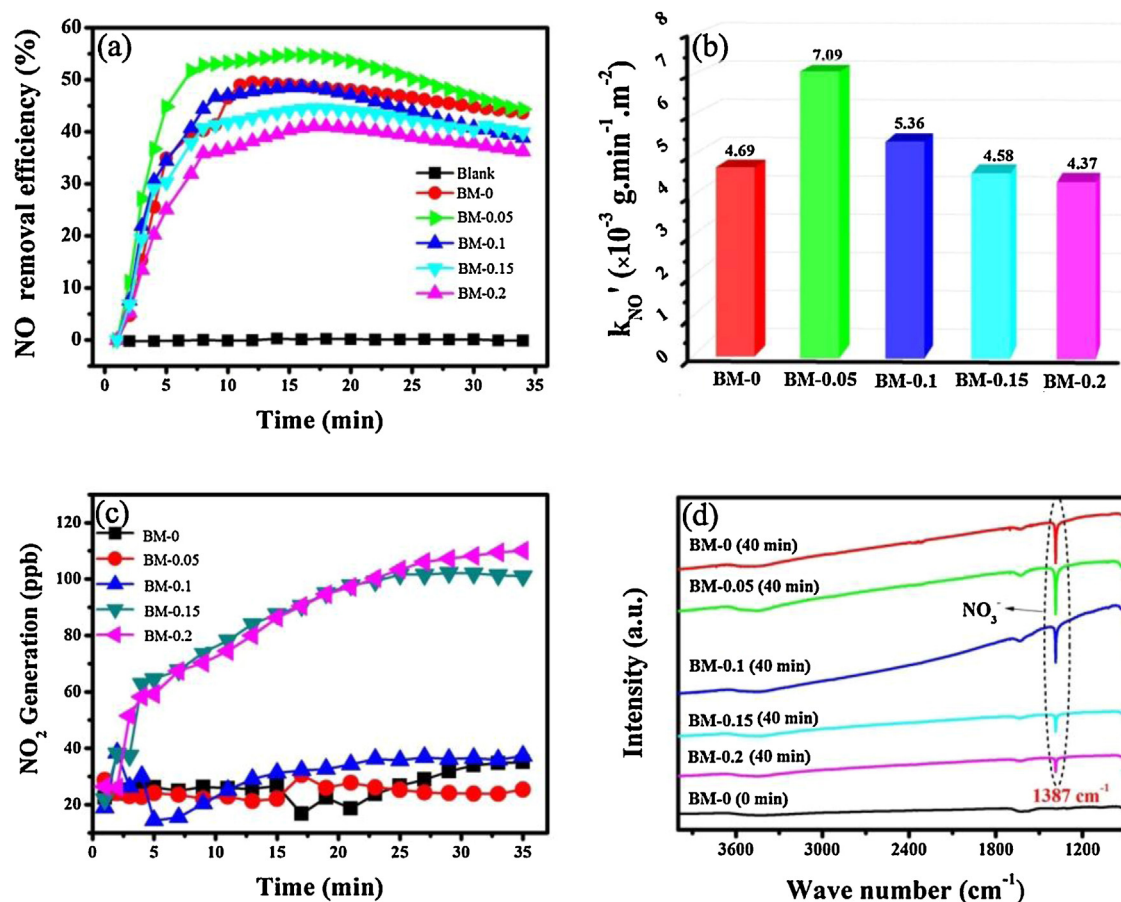


Fig. 2. (a) XPS survey spectra of BM-0 and BM-0.05 samples; high-resolution Mo 3d (b), Bi 4f (c) and O 1s spectra (d) of BM-0 and BM-0.05 samples.





**Fig. 3.** Photocatalytic removal of NO (a) and pseudo first-order kinetic constants (b) over BM- $x$  ( $x=0, 0.05, 0.1, 0.15, 0.2$ ) under visible light irradiation; monitoring of NO<sub>2</sub> intermediates during irradiation (c) and FTIR spectra of BM- $x$  ( $x=0, 0.05, 0.1, 0.15, 0.2$ ) before and after irradiation (d).

and Na<sub>2</sub>MoO<sub>4</sub>  $\times$  2H<sub>2</sub>O were mixed into 15 mL of water in a 20 mL Teflon-lined autoclave with different Bi/Mo molar ratios of 2, 2.05, 2.1, 2.15, and 2.2. The mixture was stirred for 0.5 h at room temperature in air and then kept in Teflon-lined autoclave at 160 °C for 12 h. Finally, the precipitates were collected, washed with ethanol and deionized water thoroughly, and dried at 50 °C for several hours. All these five samples were marked as BM- $x$  ( $x=0, 0.05, 0.1, 0.15, 0.2$ ).

## 2.2. Analytical methods

All theoretical calculations were performed using the plan-wave density of functional theory (DFT) with the exchange-correlation energy functional described by generalized gradient approximation using the Perdew–Burke–Ernzerhof (PBE) exchange-correlation function [33]. The calculations were implemented using the Vienna Ab-initio Simulation Package (VASP) with a plane-wave cutoff energy of 520 eV [34,35]. A (2  $\times$  2) supercell was used to simulate the molecular nitrogen activation on surfaces. During the optimizations, the energy and force converged to 10<sup>-5</sup> eV/atom and 0.02 eV/Å, respectively. The  $k$ -points were 2  $\times$  2  $\times$  2 for optimizations and increased to 7  $\times$  5  $\times$  7 for the band energy and DOS calculations of the pristine and self-doped Bi<sub>2</sub>MoO<sub>6</sub> structures. The X-ray diffraction (XRD) patterns of the samples were obtained using a Bruker D8 Advance X-ray diffractometer with Cu K $\alpha$  radiation ( $\lambda=1.5418$  nm). The morphologies and microstructures of the as-prepared samples were analyzed via scanning electron microscopy (SEM, JEOL 6700-F) and transmission electron microscopy (TEM, JEOL JEM-2010). Diffuse reflection spectra (DRS) were obtained using a Hitachi U-3310 spectrophotometer. The

Brunauer–Emmett–Teller (BET) surface areas of the powder samples were determined by nitrogen adsorption–desorption isotherm measurements at 77 K by using a Micromeritics Tristar-3000 nitrogen adsorption apparatus. The surface electronic states and Bi/Mo mole ratios of the samples were analyzed via X-ray photoelectron spectroscopy (XPS, VG Multilab 2000), and all binding energies were referenced to the C 1s peak at 284.6 eV of the surface adventitious carbon. Electron spin resonance spectra (ESR, JES-FA200, Japan) was applied to detect reactive oxygen species generated in the photocatalytic system with 5,5-dimethyl-1-pyrroline- $N$ -oxide (DMPO) as the radicals spin-trapped reagent under visible light. The photodegradation of  $p$ -nitro-blue tetrazolium chloride (NBT) was used to approximately quantify the generation of  $\cdot\text{O}_2^-$  [36]. Fourier transform infrared spectroscopy (FTIR, NICOLET IS50 FT-IR, Thermo) was employed to qualitatively detect the NO<sub>3</sub><sup>-</sup> generation on the surface of the photocatalysts during the photocatalytic removal of NO.

## 2.3. Photocatalytic activity test

The photocatalytic activities of the samples were evaluated in terms of the photocatalytic removal of NO, which was performed at ambient temperature in a continuous flow reactor. The volume of the rectangular reactor, which was made of stainless steel and covered with quartz glass window, was 4.5 L (30 cm  $\times$  15 cm  $\times$  10 cm). One sample dish with a diameter of 12.0 cm containing 0.15 g of catalyst powders was placed in the middle of the reactor, and a 30 W visible LEDs (General Electric) was vertically placed outside the reactor as a light source. The dishes coated with photocatalysts suspension with adding NBT, scavengers or not were pretreated at

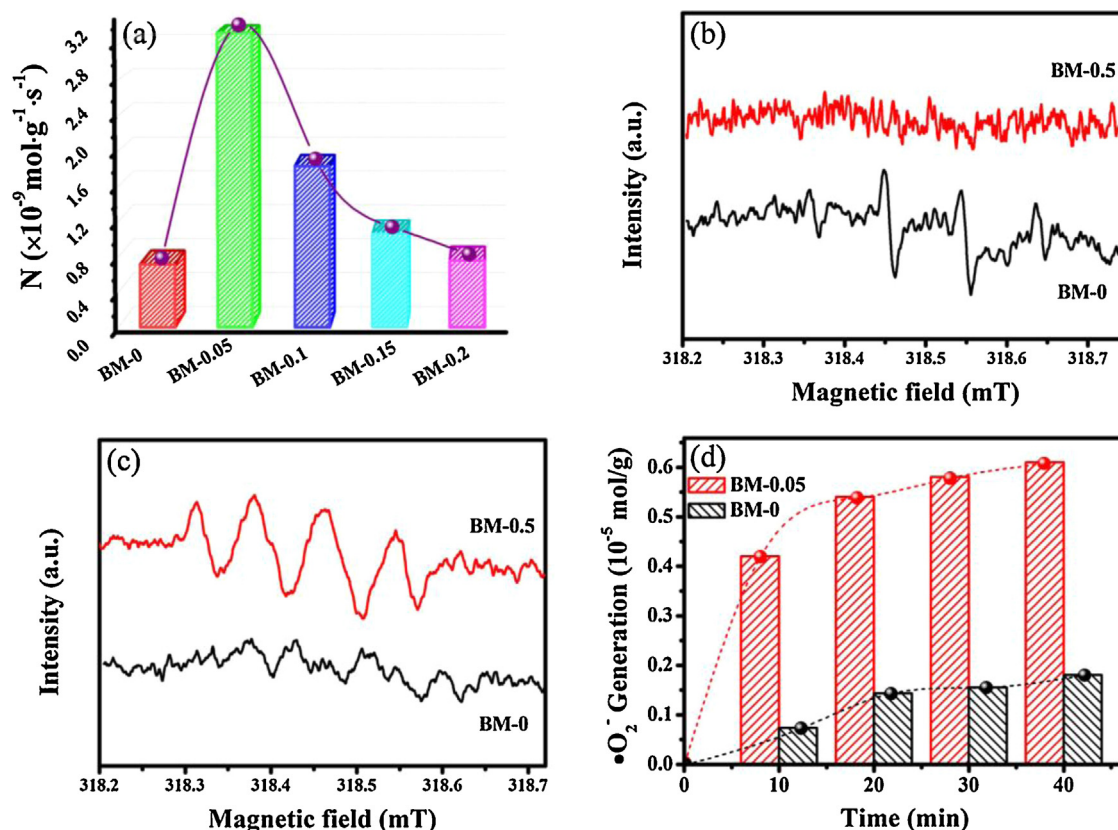


**Fig. 4.** (a) The instantaneous generation of valid hole–electron pairs ( $N$ ) on the surface of as prepared catalyst under visible light; ESR spectra of DMPO- $\bullet\text{OH}$  (b) and DMPO- $\bullet\text{O}_2^-$  (c) for BM-0 and BM-0.05 under visible light irradiation; (d) accumulation of  $\bullet\text{O}_2^-$  vs reaction time over BM-0 and BM-0.05 under visible light irradiation under moistureless conditions.

70 °C for water evaporation. The NO gas was supplied by a compressed gas cylinder at a concentration of 50 ppm NO ( $\text{N}_2$  balance) and was diluted to about 600 ppb by using a dynamic gas calibrator (Ecotech GasCal 1000) in combination with a zero air supply. The gas flow rate through the reactor was controlled at 1000 mL/min by a mass flow controller. After the adsorption–desorption equilibrium was achieved, the lamp was turned on. The concentration of NO was continuously measured using a NOx analyzer model T200 (Teledyne API). During NBT photodegradation experiment, air instead of NO was supplied continuously through the rectangular reactor. The concentration of NBT coated on samples after reaction was dissolved in water and detected with UV–vis spectrophotometer.

The removal efficiency ( $\eta$ ) of NO was calculated as follows.

$$\eta(\%) = \left(1 - \frac{C}{C_0}\right) \times 100\% \quad (8)$$

where  $C$  and  $C_0$  were the concentrations of NO in the outlet stream and the feeding stream, respectively.

#### 2.4. Photoelectrochemical experiments

The photocurrent measurement, electrochemical impedance spectroscopy (EIS) measurement and Mott–Schottky experiment were carried out in a standard three-electrode cell containing 0.5 mol/L  $\text{Na}_2\text{SO}_4$  aqueous solution with a platinum foil counter electrode and a saturated calomel electrode (SCE) as the reference electrode on a CHI 660C workstation. The working electrode was prepared as described in our previous papers [37,38]. All of the electrochemical measurements were performed at room temperature.

**Table 1**

Calculated Bader charges of the pristine (a) and self-doped (b)  $\text{Bi}_2\text{MoO}_6$ .

Element (a)	Bader charge/e	Element (b)	Bader charge/e
$\text{Bi}_1$	3.2531	$\text{Bi}_1$	3.2304
$\text{Bi}_2$	3.2531	$\text{Bi}_2$	3.7102
$\text{Mo}_3$	3.1966	$\text{Bi}_3$	2.5194
$\text{Mo}_4$	3.1966	$\text{Mo}_4$	3.1556
$\text{O}_5$	7.1354	$\text{O}_5$	7.1047
$\text{O}_6$	7.0431	$\text{O}_6$	6.8985
$\text{O}_7$	7.0431	$\text{O}_7$	7.0150
$\text{O}_8$	6.9850	$\text{O}_8$	7.1540
$\text{O}_9$	6.9686	$\text{O}_9$	7.0223

### 3. Results and discussion

#### 3.1. Theoretical calculation analysis

DFT calculations were first performed to investigate the influence of bismuth self-doping on the crystal and electronic structure of  $\text{Bi}_2\text{MoO}_6$  (Fig. 1). The crystal structure possessing unique layered structures of the pristine  $\text{Bi}_2\text{MoO}_6$  was shown in Fig. 1a, in which perovskite slabs of  $(\text{MoO}_4)^{2-}$  were sandwiched between  $(\text{Bi}_2\text{O}_2)^{2+}$  layers. The model of  $\text{Bi}_{2-x}\text{MoO}_6$  was built by replacing a Mo atom with Bi atom in a primitive cell of  $\text{Bi}_2\text{MoO}_6$  (Fig. 1b). The calculated Bader charge analysis (Table 1) revealed that the substituted Bi atom ( $\text{Bi}_4$ ) had a much smaller charge (2.5194 electrons) than Mo atoms (3.1966 electrons) and the other Bi atoms as well. Meanwhile, the Bader charges of oxygen atoms around the substituted Bi atom in  $\text{Bi}_{2-x}\text{WO}_6$  also changed correspondingly in comparison with those in the pristine  $\text{Bi}_2\text{WO}_6$ , suggesting the charge redistribution around the dopant of  $\text{Bi}_{2-x}\text{MoO}_6$ , which would change the internal electric field,

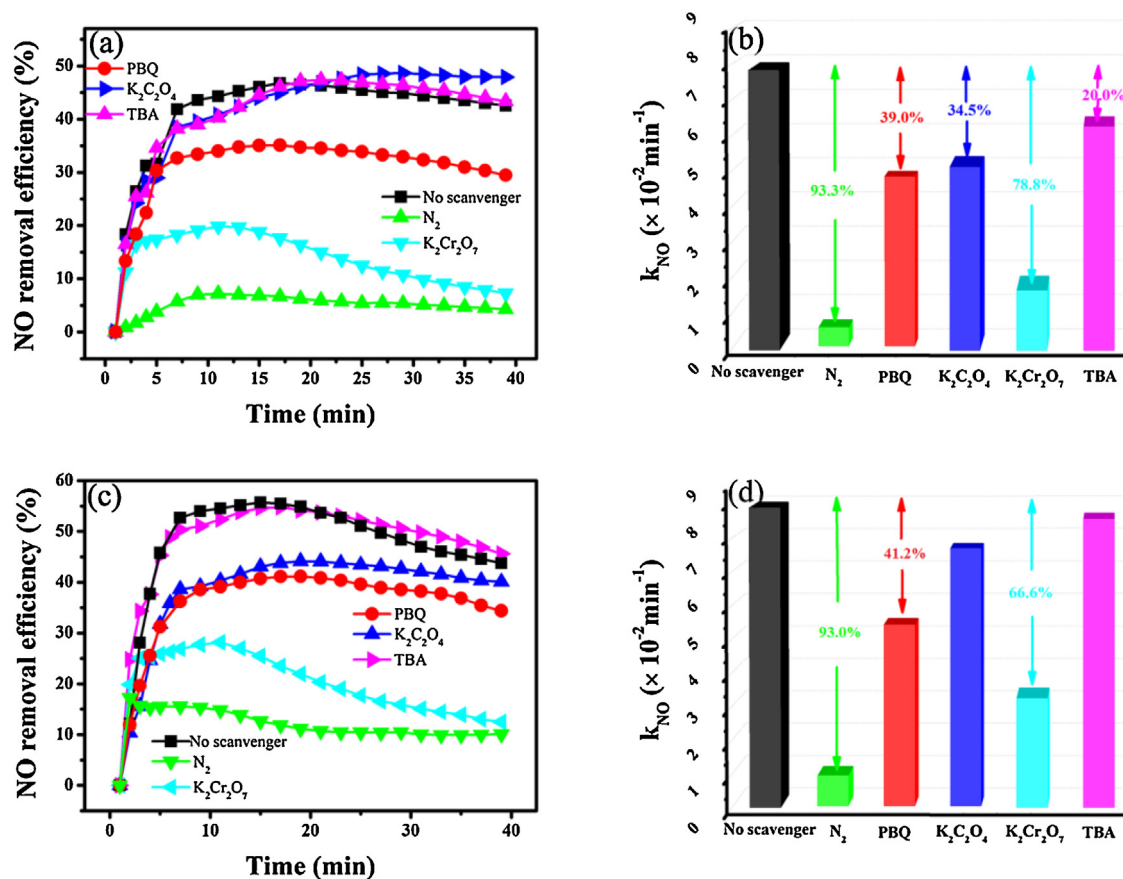


**Fig. 5.** Photocatalytic removal of NO and the corresponding pseudo first-order kinetic constants in the first 10 min over BM-0 (a and b) and BM-0.05 (c and d) under visible light irradiation with different scavengers (PBQ  $\rightarrow \cdot O_2^-$ ;  $K_2C_2O_4 \rightarrow$  hole;  $K_2Cr_2O_7 \rightarrow e^-$ ; TBA  $\rightarrow \cdot OH$ ).

**Table 2**

Bi/Mo mole ratios and BET areas of BM- $x$  ( $x=0, 0.05, 0.1, 0.15, 0.2$ ).

Sample	Bi/Mo (by XPS)	$A_{BET} (\text{m}^2 \text{ g}^{-1})$
BM-0	1.939	20.6
BM-0.05	2.042	17.9
BM-0.1	2.120	17.9
BM-0.15	2.142	17.9
BM-0.2	2.223	15.1

favoring better separation of photoexcited electrons and holes and thus improving the photocatalytic activity of  $Bi_2MoO_6$  [39]. The band structures and calculated band dispersions and densities of states displayed that the valence and conduction bands of  $Bi_{2+x}MoO_6$  were almost same as those of  $Bi_2MoO_6$  (Fig. 1c–f), but a new band composed of O 2p orbital appeared in the band gap of  $Bi_{2+x}MoO_6$ , which might favor its electron excitation. These results indicated that Bi self doping might favor photoelectron excitation of  $Bi_2MoO_6$  and improve the separation and transmission of its photoexcited electron–hole pairs.

### 3.2. Characterization of the samples

The XRD patterns of the as-prepared powders showed that all samples appeared to be phase-pure  $Bi_2MoO_6$  (JCPDS No. 84-787) (Fig. S1a in the SM). The slightly shifted (1 3 1) diffraction peaks in the range of  $2\theta = 28\text{--}29^\circ$  with increasing Bi doping content toward a higher  $2\theta$  value can be attributed to the formation of molybdenum vacancies after Bi self-doping (Fig. S1b in the SM). The SEM and TEM images of the as-synthesized photocatalyst exhibited that all the samples consisted of homogeneous nanoplates with width of

30–100 nm and thickness of about 10 nm, indicating that Bi doping did not significantly affect the morphology and crystal sizes of  $Bi_2MoO_6$  (Fig. S2 and S3 in the SM). The HRTEM image and fast Fourier transform (FFT) patterns of BM-0 and BM-0.05 revealed that both of them were exposed with the (0 1 0) crystal planes (Fig. S3c and S3d in the SM). XPS analysis of the as-prepared BM-0 and BM-0.05 illustrated that these two samples were composed of Mo, Bi, O, and a trace amount of adventitious carbon (Fig. 2). The symmetric Mo 3d peaks of the two samples at 235.4 and 232.3 eV can be ascribed to Mo 3d 3/2 and Mo 3d 5/2 of  $MoO_4^{2-}$ , respectively (Fig. 2b) [40]. For self-doped  $Bi_2MoO_6$ , two new peaks appeared at 160.3 and 165.8 eV, which can be assigned to  $Bi^{3+x+}$  ( $Bi^{4+}$  or  $Bi^{5+}$ ) (Fig. 2c) [41]. Meanwhile, the intensity of the Bi–O peak at 531.8 eV increased for BM-0.05, thereby indicating that the Bi–O bond was strengthened after Bi self-doping (Fig. 2d). This result confirmed that bismuth was thoroughly introduced into the  $Bi_2MoO_6$  lattice. Combining the results of theoretical calculation, XRD analysis, SEM, TEM observation, as well as Bi/Mo mole ratio measurement by XPS (Table 2), we inferred that Bi can be doped in  $Bi_2MoO_6$  successfully through a soft-chemical method which might facilitate its electron excitation and photoexcited electron–hole separation without altering its crystal sizes, preferential crystal orientations, and morphology.

### 3.3. Effect of Bi self-doping on NO<sub>x</sub> removal

The photocatalytic activities of all BM- $x$  ( $x=0, 0.05, 0.1, 0.15, 0.2$ ) samples was tested to investigate the influence of Bi self-doping on the activity performance of  $Bi_2MoO_6$  through the photocatalytic removal of NO under visible light ( $\lambda > 420 \text{ nm}$ ) irradiation. Fig. 3a,b



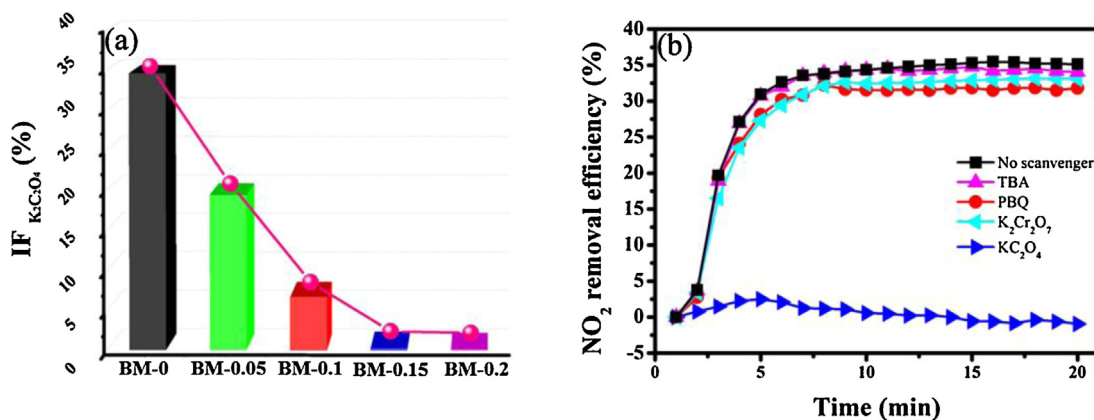


**Fig. 6.** (a) The inhibition factor (IF) of  $K_2C_2O_4$  during the photocatalytic removal of NO over BM- $x$  ( $x = 0, 0.05, 0.1, 0.15, 0.2$ ); (b) photocatalytic removal of  $NO_2$  over BM-0.05 under visible light irradiation with different scavengers ( $PBQ \rightarrow \cdot O_2^-$ ;  $K_2C_2O_4 \rightarrow \text{hole}$ ;  $K_2Cr_2O_7 \rightarrow e^-$ ;  $TBA \rightarrow \cdot OH$ ).

illustrated the NO removal efficiency as a function of time and the corresponding NO removal rate in the first 10 min (Fig. S4a in the SM). It can be found that all five as-prepared samples exhibited fairly high NO removal efficiency, among which BM-0.05 possessed the best photocatalytic activity even after surface normalization. The NO removal rate first increased with Bi self-dopant amount and then slightly decreased gradually since  $x = 0.1$ . The reaction intermediate  $NO_2$  determination during photocatalytic removal of NO showed that BM-0, BM-0.05 and BM-0.1 exhibited a quite low accumulation of  $NO_2$  (Fig. 3c). However, when the self-doping amount was further increased ( $x > 0.1$ ), the concentration of  $NO_2$  raised

sharply with the time, thereby implying that the deep oxidation of NO might be suppressed. All these five samples after photocatalytic tests were collected and analyzed by FTIR (Fig. 3d and Fig. S4b in the SM), which exhibited that the peak at  $1387\text{ cm}^{-1}$  ascribed to the antisymmetric stretching vibration absorption of  $NO_3^-$  of BM-0.15 and BM-0.2 was significantly weaker than those of the other three samples, indicating that the  $NO_2 \rightarrow NO_3^-$  oxidation process over BM-0.15 and BM-0.2 might be restrained. This was further confirmed by the direct photocatalytic removal  $NO_2$  (Fig. S4c in the SM), which displayed that the  $NO_2$  removal efficiency decreased gradually with Bi doping amount. These results demonstrated that

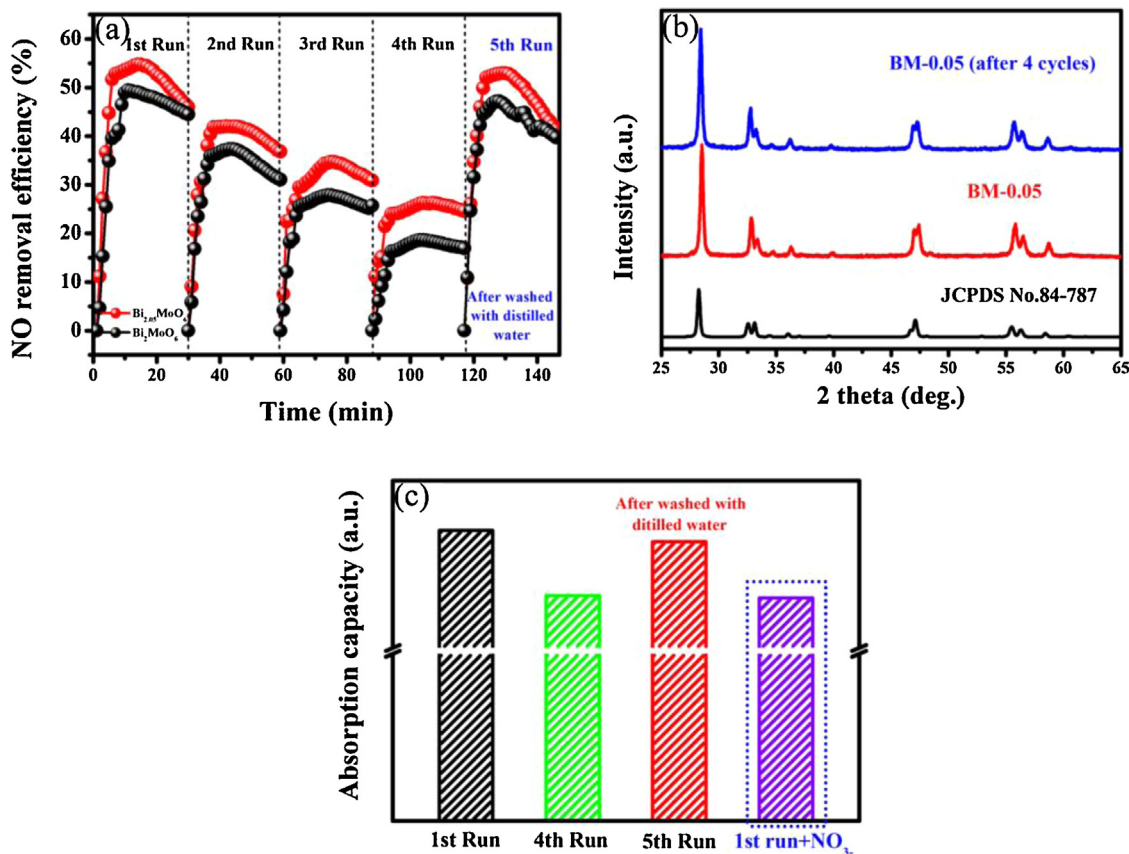


**Fig. 7.** (a) Cycling runs for photocatalytic oxidation of NO over BM-0 and BM-0.05; (b) XRD patterns of BM-0.05 before or after 4 cycles of NO removal test; (c) NO absorption capacity of BM-0.05 under different conditions during the dark absorption process.

the  $\text{NO}_2 \rightarrow \text{NO}_3^-$  oxidation process was restrained during the photocatalytic removal of NO over a high amount of Bi self-doped  $\text{Bi}_2\text{MoO}_6$ .

### 3.4. Effect of Bi self-doping on reactive species generation

We subsequently utilized the photocurrent generation and ESR spin-trap with DMPO technique to identify and determine the reactive species generated over BM- $x$  ( $x=0, 0.05, 0.1, 0.15, 0.2$ ) samples during photocatalysis process under visible light irradiation (Fig. 4 and Fig. S5a in the SM). The instantaneous generation of valid hole–electron pairs (N) on the surface of as prepared catalyst under visible light was calculated using the Eq. (9).

$$N(\text{mol} \times \text{g}^{-1} \times \text{s}^{-1}) = \frac{Q_t}{F \times t \times m} = \frac{\int_0^t I(t) dt \times S}{F \times t \times m} \quad (9)$$

where  $Q_t$  (C) is the total electric quantity produced during the illumination of visible light, which can be further calculated by photocurrent integration from time 0 to  $t$  (s).  $M$  (g) and  $S$  ( $\text{m}^{-2}$ ) are the catalysts mass and electrode area, respectively.  $F$  is the Faraday constant (96,485.3 C/mol).

It was found that all the four self-doped BM- $x$  ( $x=0, 0.05, 0.1, 0.15, 0.2$ ) could produce more available hole–electron pairs than the pristine  $\text{Bi}_2\text{MoO}_6$  (Fig. 4a and Fig. S5a in the SM) under visible light illumination, indicating that Bi self-doping enhanced the separation of photogenerated holes and electrons as well as its charge transport characteristic (Fig. S5b in the SM). It was noted that this enhancement first increased with Bi self dopant amount and then decreased gradually. This can be attributed to the formation of carrier-recombination centers result from superabundant Bi doping [42]. BM-0.05 possessed the largest amount of valid hole–electron pairs which was almost 4 times than that of the pristine  $\text{Bi}_2\text{MoO}_6$ , implying that more hole–electron pairs could participate in NO removal after Bi self-doping. ESR spectra of BM-0 and BM-0.05 exhibited that the distinctive characteristic peaks of DMPO- $\bullet\text{OH}$  were observed only in the visible light irradiated BM-0 suspension (Fig. 4b) while a much stronger DMPO- $\bullet\text{O}_2^-$  signals was photogenerated by BM-0.05 than BM-0 (Fig. 4c). According to the results of the UV–vis absorption spectra and Mott–Chottky plots of BM- $x$  ( $x=0, 0.05, 0.1, 0.15, 0.2$ ) samples (Fig. S6 in the SM), the conduction band potentials of the pristine BM-0 and BM-0.05 were calculated to be about  $-0.33$  and  $-0.38$  eV vs NHE, respectively. Accordingly, the valence band potentials of these two samples were calculated to be 2.39 and 2.34 eV, demonstrating the band positions of  $\text{Bi}_2\text{MoO}_6$  slightly transferred toward a lower energy level after Bi self-doping spite of their unchanged intrinsic optical properties and band gaps. With a much lower valence band potential (2.34 eV vs NHE), hence, BM-0.05 is not capable of oxidizing water or surface hydroxyl group to form  $\bullet\text{OH}$  (2.38 eV vs NHE). Nevertheless, both BM-0 and BM-0.05 have a suitable conduction band potentials to trap molecular  $\text{O}_2$  with photogenerated electrons to generate  $\bullet\text{O}_2^-$  ( $-0.33$  eV vs NHE). NBT degradation experiment was subsequently carried out under moistureless condition to compare the  $\bullet\text{O}_2^-$  accumulation over these two samples (Fig. 4d), which indicated that BM-0.05 generate about four times of  $\bullet\text{O}_2^-$  ( $0.61 \times 10^{-5} \text{ mol} \times \text{g}^{-1}$ ) than BM-0 ( $0.15 \times 10^{-5} \text{ mol} \times \text{g}^{-1}$ ) in 40 min. This can be attributed to electron reducing power enhancement, improved electron excitation property (Fig. S5a in the SM), and better charge transfer characteristic (Fig. S5b in the SM). Therefore, we concluded that Bi self-doping can significantly improve the generation of  $\bullet\text{O}_2^-$  and holes while depress the formation of  $\bullet\text{OH}$ , which offered us a perfect opportunity to tune reactive species generation during photocatalysis and investigate their different functions in NO removal.

### 3.5. The photocatalytic mechanism of NO<sub>x</sub> removal

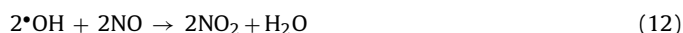
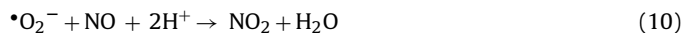
As mentioned before, little has changed about the crystal sizes, preferential crystal orientations, morphology, surface area and intrinsic optical properties of  $\text{Bi}_2\text{MoO}_6$  after Bi self doping except for reactive species generation, according to the previous characterization analysis and BET areas measurement (Table 2). In order to figure out the specific effect of Bi self doping on NO removal mechanism, we tried to clarify the function of the active species during the photocatalytic removal of NO and determined the influence of self-doping on NO photocatalytic removal mechanism over  $\text{Bi}_2\text{MoO}_6$  by photocatalytic removal of NO over BM-0 and BM-0.05 with  $\text{Na}_2\text{C}_2\text{O}_4$ ,  $\text{K}_2\text{Cr}_2\text{O}_7$ , *tert*-butyl alcohol (TBA) and *p*-benzoquinone (PBQ) as hole,  $\text{e}^-$ ,  $\bullet\text{OH}$ , and  $\bullet\text{O}_2^-$  scavengers, respectively (Fig. 5a,c and Fig. S7 in the SM). For both BM-0 and BM-0.05, the addition of the  $\text{K}_2\text{Cr}_2\text{O}_7$  had a dramatic negative effect on NO removal, implying that photoelectrons played an indispensable role in NO photocatalytic removal over these two samples. Besides, the NO removal was almost completely restrained when  $\text{O}_2$  was excluded with  $\text{N}_2$  (Fig. S7c), thereby demonstrating that the photogenerated electrons participated in this photocatalytic process over both BM-0 and BM-0.05 by trapping molecular oxygen to generate  $\bullet\text{O}_2^-$  indirectly through the  $\text{NO} \rightarrow \text{NO}_2 \rightarrow \text{NO}_3^-$  oxidation process rather than the direct  $\text{NO} \rightarrow \text{N}_2$  reduction process, which was further confirmed by the apparent retardation on NO removal after adding PBQ to capture  $\bullet\text{O}_2^-$ . For BM-0.05, it is worth noting that the presence of TBA had an imperceptible influence on NO decay, whereas it inhibited about 20% of NO removal for BM-0 (Fig. 5b,d), thereby indicating that the contribution of  $\bullet\text{OH}$  on NO removal over BM-0 was weakened after Bi self-doping because the valence band potential of self-doped  $\text{Bi}_2\text{MoO}_6$  is not positive enough to oxidize the water or surface hydroxyl group to form  $\bullet\text{OH}$  to participate in the reaction, which is consistent with the ESR results. In addition, a minor retardation of 19.7% occurred when the holes were captured by  $\text{K}_2\text{C}_2\text{O}_4$  during NO photocatalytic removal over BM-0.05, which was much smaller than that over the pristine  $\text{Bi}_2\text{MoO}_6$  (39.0%). Correspondingly, NO removal suppression over BM-0.05 increased to 41.4% from 39% in absence of  $\bullet\text{O}_2^-$  in comparison with that over BM-0, meaning that the contribution of  $\bullet\text{O}_2^-$  on NO photocatalytic removal over BM-0 increased after Bi self-doping spite of the eclipsed function of  $\text{h}^+$  (Fig. 6a).

From the comparison of  $\text{NO}_2$  and  $\text{NO}_3^-$  generation during the photocatalytic removal of NO in the presence of different scavengers (Fig. S8 in the SM), it can be found that the  $\text{NO}_2$  concentration significantly increased in the existence of  $\text{K}_2\text{C}_2\text{O}_4$  especially for BM-0 while the intensity of  $\text{NO}_3^-$  infrared characteristic absorption peak decreased remarkably (Fig. S8 in the SM), indicating that the photogenerated holes had an essential function in  $\text{NO}_2$  oxidation. Nevertheless, the addition of PBQ had little effect on  $\text{NO}_2$  generation, thereby implying  $\bullet\text{O}_2^-$  might not contribute much to the further oxidation of  $\text{NO}_2$  to  $\text{NO}_3^-$ . For BM-0, a mild increase was also observed in  $\text{NO}_2$  generation in the presence of TBA, thereby suggesting that  $\bullet\text{OH}$  was also involved in  $\text{NO}_2$  oxidation (Fig. S8a in the SM). Fig. 6b shows the photocatalytic removal of  $\text{NO}_2$  over BM-0.05 with these different scavengers. It was noted that  $\text{NO}_2$  oxidation was almost completely restrained when holes were captured by  $\text{Na}_2\text{C}_2\text{O}_4$  spite of the little effluence of PBQ, TBA, and  $\text{K}_2\text{Cr}_2\text{O}_7$ . These results further confirmed that  $\bullet\text{O}_2^-$  played indispensable role in NO to  $\text{NO}_2$  oxidation process while photogenerated holes were the crucial active species to oxidize  $\text{NO}_2$ – $\text{NO}_3^-$ .

Hence, we can conclude that  $\bullet\text{O}_2^-$  originated from the reaction of oxygen and photogenerated electrons mainly participated in the oxidation of NO to  $\text{NO}_2$  through Eq. (8) during the photocatalytic removal of NO over the pristine  $\text{Bi}_2\text{MoO}_6$ . The photogenerated holes and  $\bullet\text{OH}$  functioned as the key oxidative species in the further oxidation of  $\text{NO}_2$  to  $\text{NO}_3^-$  through Eqs. (12)–(14). For self-doped



$\text{Bi}_2\text{MoO}_6$ , Bi self-doping enhanced the generation of  $\bullet\text{O}_2^-$  (Eq. (4)) and thus favored NO removal by accelerating the first step of NO oxidation (Eq. (10)). On the contrary, the weakened oxidative ability of the photogenerated holes after self-doping hindered the further oxidation of  $\text{NO}_2$  (Eq. (13)) and then indirectly restrained the NO removal, thereby gradually decreasing its contribution with the doping amount of bismuth (Fig. 6a). That is why the NO removal was slightly blocked as the reaction time increased especially for BM- $x$  ( $x=0.1, 0.15, 0.2$ ) samples (Fig. 3a). Therefore, BM-0.05, with an optimal Bi self-doping amount ( $x=0.05$ ), possessed the best photocatalytic NO removal efficiency due to the enhancement of  $\bullet\text{O}_2^-$  generation and enough holes' participation, which improved its photocatalytic ability to the greatest extent.



### 3.6. Photostability of BM- $x$ during NO $_x$ removal

The stability and recyclability of BM- $x$  ( $x=0, 0.5$ ) was subsequently evaluated through the multiple runs of photocatalytic experiments with the used BM-0.05 photocatalyst (Fig. 7a). The recycling test revealed that the NO removal efficiency over BM- $x$  ( $x=0, 0.5$ ) decayed significantly with the cycling times, implying that BM- $x$  ( $x=0, 0.5$ ) might be deactivated by NO oxidation intermediate like  $\text{NO}_3^-$ . After 4 repeated runs of photocatalytic test, almost 30% of NO removal efficiency decreased for BM-0 which was much larger than that for BM-0.05 (20%), indicating that the deactivation of  $\text{Bi}_2\text{MoO}_6$  was suppressed after Bi self-doping. In spite of the deactivation, the catalytic ability of BM-0.05 almost completely recovered after regenerating with distilled water. To figure out the cause of this deactivation, we analyzed and compared the XRD patterns of BM-0.05 samples before and after photocatalytic reaction, which indicated that the crystal structure of BM-0.05 did not change after visible light irradiation and thus excluded the presence of photo-corrosion (Fig. 7b). The NO absorption capacity of BM-0.05 in the presence of  $\text{NO}_3^-$  or not were subsequently compared during the dark absorption process (Fig. 7c). It was noted that BM-0.05 without any treatment possessed the largest NO absorption capacity. But it is absorptivity on NO obviously declined after four cycling runs' photocatalytic reaction. Moreover, the addition of  $\text{NO}_3^-$  also significantly hindered the NO absorption of BM-0.05. All these results and indicated that  $\text{NO}_3^-$ , the oxidation product of NO during the photocatalytic process, might occupied the absorption site of NO, impeding the contact between NO and catalysts, and further inhibiting the photocatalytic oxidation of NO under visible light irradiation. In spite of this, BM-0.05 catalyst can be effectively regenerated and keep a high NO removal efficiency again after washed with water.

## 4. Conclusions

In summary, the reactive species regulation over  $\text{Bi}_2\text{MoO}_6$  under visible light can be realized through a Bi self-doping technology via a simple soft-chemical method. Density functional theory calculations and systematical characterization results revealed that Bi self-doping could not only promote the separation and transfer of photogenerated electron-hole pairs of  $\text{Bi}_2\text{MoO}_6$  but also alter the position of valence and conduction band without changing its preferential crystal orientations, morphology, visible light absorption as well as band gap energy. The photocatalytic removal of

NO and products determination revealed that the enhanced generation of superoxide could improve the oxidation of NO to  $\text{NO}_2$ .  $\bullet\text{OH}$  and photogenerated holes mainly contributed to the further oxidation of  $\text{NO}_2$  to  $\text{NO}_3^-$ . Photostability and NO absorption tests demonstrated that  $\text{NO}_3^-$  on the surface of catalysts took up the NO absorption sites and thus caused the deactivation of catalysts. This study provides new insight into the different effects of photo-generated reactive species on NO removal and sheds light on the design of highly efficient visible light-driven photocatalysts for NO removal.

## Acknowledgements

This research is mainly financially supported by the research grant of Early Career Scheme (ECS 809813) from the Research Grant Council, Hong Kong SAR Government. This work was supported from our collaborators by National Natural Science Funds for Distinguished Young Scholars (Grant 21425728), National Basic Research Program of China (973 Program) (Grant 2013CB632402), National Science Foundation of China (Grants 21177048, and 51472100), National Natural Science Foundation of China (51572101), Key Project of Natural Science Foundation of Hubei Province (Grant 2013CFA114), Self-Determined Research Funds of CCNU from the Colleges' Basic Research and Operation of MOE (Grant CCNU14Z01001), and Excellent Doctorial Dissertation Cultivation Grant from Central China Normal University (Grant 2013YBYB56). We also thank the National Supercomputer Center in Jinan for providing high-performance computation.

## Appendix A. Supplementary data

Supplementary data associated with this article can be found, in the online version, at <http://dx.doi.org/10.1016/j.apcatb.2015.09.046>.

## References

- [1] Z. Ai, W. Ho, S. Lee, J. Phys. Chem. C 115 (2011) 25330–25337.
- [2] J. Ma, H. Wu, Y. Liu, H. He, J. Phys. Chem. C 118 (2014) 7434–7441.
- [3] M. Ou, F. Dong, W. Zhang, Z. Wu, Chem. Eng. J. 255 (2014) 650–658.
- [4] G. Li, D. Zhang, J.C. Yu, M.K.H. Leung, Environ. Sci. Technol. 44 (2010) 4276–4281.
- [5] A. Satinder, Am. Chem. Soc. (2013) 1–14.
- [6] X. Zhang, C. Chen, P. Lin, A. Hou, Z. Niu, J. Wang, Environ. Sci. Technol. 45 (2010) 161–167.
- [7] Environ. Sci. Technol. 36 (5) (2002) 97A–97A.
- [8] J. Darweesh, J. Chem. Educ. 60 (1983) 686.
- [9] C. Su, X. Ran, J. Hu, C. Shao, Environ. Sci. Technol. 47 (2013) 11562–11568.
- [10] D.S. Bhatkhande, V.G. Pangarkar, A.A.C.M. Beenackers, J. Chem. Technol. Biotechnol. 77 (2002) 102–116.
- [11] J. Ma, W. Ma, W. Song, C. Chen, Y. Tang, J. Zhao, Y. Huang, Y. Xu, L. Zhang, Environ. Sci. Technol. 40 (2005) 618–624.
- [12] I. Schmidt, O. Sliemers, M. Schmid, E. Bock, J. Fuerst, J.G. Kuenen, M.S. Jetten, M. Strous, FEMS Microbiol. Rev. 27 (2003) 481–492.
- [13] Q. Wu, R. van de Krol, J. Am. Chem. Soc. 134 (2012) 9369–9375.
- [14] M. Matsuoka, S. Higashimoto, H. Yamashita, M. Anpo, Res. Chem. Intermed. 26 (2000) 85–92.
- [15] J. Lasek, Y.-H. Yu, J.C.S. Wu, J. Photochem. Photobiol. C: Photochem. Rev. 14 (2013) 29–52.
- [16] W.S. Ju, M. Matsuoka, M. Anpo, Catal. Lett. 71 (2001) 91–93.
- [17] Z. Ai, S. Lee, Appl. Surf. Sci. 280 (2013) 354–359.
- [18] S. Ge, L. Zhang, Environ. Sci. Technol. 45 (2011) 3027–3033.
- [19] F. Dong, Z. Wang, Y. Li, W.K. Ho, S.C. Lee, Environ. Sci. Technol. 48 (2014) 10345–10353.
- [20] R. Sugrañez, J. Balbuena, M. Cruz-Yusta, F. Martín, J. Morales, L. Sánchez, Appl. Phys. B: Environ. 165 (2015) 529–536.
- [21] X. Ding, X. Song, P. Li, Z. Ai, L. Zhang, J. Hazard. Mater. 190 (2011) 604–612.
- [22] F. Zuo, L. Wang, T. Wu, Z. Zhang, D. Borchardt, P. Feng, J. Am. Chem. Soc. 132 (2010) 11856–11857.
- [23] Y. Shi, P.F. Ndione, L.Y. Lim, D. Sokaras, T.C. Weng, A.R. Nagaraja, A.G. Karydas, J.D. Perkins, T.O. Mason, D.S. Ginley, A. Zunger, M.F. Toney, Chem. Mater. 26 (2014) 1867–1873.
- [24] C.C. Han, C.H. Lu, S.P. Hong, K.F. Yang, Macromolecules 36 (2003) 7908–7915.
- [25] J. Wang, S. Su, B. Liu, M. Cao, C. Hu, Chem. Commun. 49 (2013) 7830–7832.

- [26] M. Sun, Y. Su, C. Du, Q. Zhao, Z. Liu, *RSC Adv.* 4 (2014) 30820–30827.
- [27] F. Zuo, L. Wang, T. Wu, Z. Zhang, D. Borchardt, P. Feng, *J. Am. Chem. Soc.* 132 (2010) 11856–11857.
- [28] X. Zhang, L. Zhang, *J. Phys. Chem. C* 114 (2010) 18198–18206.
- [29] G. Dong, K. Zhao, L. Zhang, *Chem. Commun.* 48 (2012) 6178–6180.
- [30] Y. Shimodaira, H. Kato, H. Kobayashi, A. Kudo, *J. Phys. Chem. B* 110 (2006) 17790–17797.
- [31] J.F. Brazdil, D.D. Suresh, R.K. Grasselli, *J. Catal.* 66 (1980) 347–367.
- [32] Y.H. Han, W. Ueda, Y. Moro-Oka, *J. Catal.* 186 (1999) 75–80.
- [33] J.P. Perdew, K. Burke, M. Ernzerhof, *Phys. Rev. Lett.* 77 (1996) 3865–3868.
- [34] G. Kresse, J. Furthmüller, *Phys. Rev. B* 54 (1996) 11169–11186.
- [35] G. Kresse, D. Joubert, *Phys. Rev. B* 59 (1999) 1758–1775.
- [36] B.H.J. Bielski, G.G. Shiue, S. Bajuk, *J. Phys. Chem.* 84 (1980) 830–833.
- [37] J. Wang, Y. Yu, L. Zhang, *Appl. Phys. B: Environ.* 136–137 (2013) 112–121.
- [38] J. Jiang, K. Zhao, X. Xiao, L. Zhang, *J. Am. Chem. Soc.* 134 (2012) 4473–4476.
- [39] W.J. Jo, J.W. Jang, K. Kong, H.J. Kang, J.Y. Kim, H. Jun, K.P.S. Parmar, J.S. Lee, *Angew. Chem. Int. Ed.* 51 (2012) 3147–3151.
- [40] H. Li, J. Liu, W. Hou, N. Du, R. Zhang, X. Tao, *Appl. Phys. B: Environ.* 160–161 (2014) 89–97.
- [41] X. Ding, K. Zhao, L. Zhang, *Environ. Sci. Technol.* 48 (2014) 5823–5831.
- [42] R. Asahi, T. Morikawa, T. Ohwaki, K. Aoki, Y. Taga, *Science* 293 (2001) 269–271.